Available online at www.sciencedirect.com
SCIENCE DIRECT®
Journal of Solid State Chemistry 179 (2006) 830–835
JOURNAL OF SOLID STATE CHEMISTRY
www.elsevier.com/locate/jssc

# Synthesis, structure, and properties of four ternary compounds: CaSr*Tt*, *Tt* = Si, Ge, Sn, Pb

Shengfeng Liu, John D. Corbett*

*Ames Laboratory,[1] Department of Chemistry, Iowa State University, Ames, Iowa 50010, USA*

Received 13 October 2005; received in revised form 23 November 2005; accepted 4 December 2005
Available online 9 January 2006

**Abstract**

The title compounds were synthesized and characterized by structural measurements and electronic structure calculations. Single-crystal X-ray diffraction analyses established that they all have the orthorhombic *inverse*-$PbCl_2$-type structure (*Pnma*, $Z = 4$, $a = 8.108(2)$, $8.124(2)$, $8.421(2)$, $8.509(2)$ Å; $b = 4.944(1)$, $4.949(1)$, $5.168(1)$, $5.189(1)$ Å; $c = 9.170(2)$, $9.184(2)$, $9.685(2)$, $9.740(2)$ Å, respectively). The tetrel (*Tt*) atoms are situated in tricapped trigonal prisms of ordered Sr and Ca atoms in which the smaller Ca atoms play a distinctive role. The structure is distinguishable from the $Co_2Si$ type by its more nearly ideal 6 + 3 (TCTP) environment about *Tt* rather than a higher coordination by cations. Other representations of the two structural types are also considered. Electronic band structure calculations suggest that the compounds are semiconductors, in agreement with literature data on their $Ae_2Tt$ analogues.


*Keywords:* Tetrelide phase; Crystal structure; Synthesis; Inverse $PbCl_2$ structure type

## 1. Introduction

Reductions of the triel (group 13—*Tr*) or tetrel (group 14—*Tt*) elements by alkali or alkaline-earth metals (*Ae*) often lead to a variety of polar intermetallic compounds that have elicited considerable interest. The tetrels often yield Zintl (valence) compounds that are semiconductors. Although the more common cluster compounds of the triels appear to be electron-precise Zintl phases, they are frequently metallic rather than semiconducting [1,2]. Another novel feature is that the presence of mixed cations of different sizes, charges, or both frequently provides new and unusual structures within the same systems. This appears particularly true when polyanions are involved because bonding in these intermetallics appears to be governed by good packing and optimized Madelung energies. For instance, only alkali-metal–triel phases with mixed cations have been found to yield isolated, centered $Tl_{13}^{10-}$ and $Tl_{13}^{11-}$ icosahedra in the compositions $Na_4A_6In_{13}$ ($A$ = K,Rb,Cs) and $Na_3K_8In_{13}$ [3], respectively, as well as closo- and arachno-$In_{12}$ in $Na_{26}A_3In_{48}$ ($A$ = K–Cs) [4], and closo-$In_{12}$ and open $In_{15}$ in $Na_{4.8}K_{18.2}In_{39}$ [5].

Explorations of the less-studied alkaline-earth-metal–triel systems have revealed a greater dominance of network phases. In $SrIn_4$ [6] and $BaAuTl_3$ [7], for example, good accommodation of the dipositive cations is a substantial factor in the nature of the network substructures achieved. Mixed alkaline-earth-metal compounds with the tetrel elements have received only limited exploration in this regard. In one instance, this circumstance was found to uniquely stabilize $Ca_{6.2}Mg_{3.8}Sn_7$ [8] with its novel chains of square planar tin units, and another composition in the same system yielded the first $W_5Si_3$-type derivatives in these systems [9]. Here we describe a further exploration of ternary alkaline-earth-metal–tetrel systems with mixed cations that have led to four new but not entirely unusual phases CaSrSi, CaSrGe, CaSrSn, and CaSrPb.

*Corresponding author. Fax: +1 515 294 6789.
*E-mail address:* jcorbett@iastate.edu (J.D. Corbett).
[1]This research was supported by the Office of Basic Energy Sciences, Materials Sciences Division, US Department of Energy (DOE). The Ames Laboratory is operated for DOE by Iowa State University under Contract No. W-7405-Eng-82. Accordingly, the US Government retains a nonexclusive, royalty-free license to publish or reproduce the published contribution, or to allow others to do so for US Government purposes.

0022-4596/$ - see front matter © 2005 Elsevier Inc. All rights reserved.
doi:10.1016/j.jssc.2005.12.006

## 2. Experimental section

### 2.1. Syntheses

All reactions were allowed to take place in welded Nb tubes that were in turn jacketed in a fused silica container following techniques described previously [6–9]. The elements Ca (99.99%), Sr (99.9%), Si (99.9%), Sn (99.999%), all from Alfa-Aesar, Ge (99.99%, Johnson-Matthey), and Pb (99.9999%, Cominco Products, electrolytic bar) were employed. All materials were handled in $N_2$- or He-filled gloveboxes with moisture levels below 0.1 ppm by volume.

Single crystals of CaSrSn were first obtained following an attempt to prepare a ternary phase $Ca_4SrSn_3$ (as a possible $Cr_5B_3$ type). The reaction mixtures were held for 4 h at 1100 °C, quenched in water, then equilibrated at 550 °C for 10 days, and finally cooled to room temperature at 5 °C/h. After the structure and stoichiometry of CaSrSn had been established, single crystals and single-phase samples (>95%) of all four were achieved via similar stoichiometric reactions. Comparison of individual reaction products according to their Guinier powder patterns with those calculated from the refined structures led to these >95% purity assessments, 5% being a conservative estimate of the detectibility of a second phase. X-ray patterns from powdered samples mounted with a little bit of vacuum grease between pieces of cellophane tape were collected with the aid of an Enraf-Nonius 552 Guinier camera, Cu $K\alpha$ radiation ($\lambda = 1.540562$ Å), and NIST silicon as an internal standard. The crystals are all silvery and gray when finely ground.

### 2.2. Properties

Electrical resistivity measurements of CaSrSn were attempted at 34 MHz over 110–250 K by the electrodeless Q method with the aid of a Hewlett-Packard 4342A Q meter [10]. For this purpose, 80.9 mg of a powdered CaSrSn sample with grain diameters between 150 and 250 μm was dispersed with chromatographic alumina and sealed under He in a Pyrex tube. However, the resistivities were too large to give an answer by this method (>some hundreds of μΩ cm), unlike CaMgSn in the same structure which is a poor metal. Small amounts of paramagnetic impurities prevented our usual simple test of the same phase for the diamagnetism of the expected semiconductor, as opposed to the Pauli paramagnetism of a metallic phase.

### 2.3. Structure determinations

Block-shaped crystals were selected in the glovebox and sealed into thin-walled glass capillaries. The crystals were first checked by Laue photographs to determine which were most suitable for structural studies. Diffraction data sets were collected at 23 °C with the aid of a Bruker APEX SMART CCD diffractometer with monochromated Mo $K\alpha$ radiations. A total of 1315 frames were collected for each with an exposure time of 10 s/frame. The diffracted intensities were integrated with the SAINT subprogram in the SMART software package [11]. The XPREP subprogram in SHELXTL [12] was used for the space group determinations which according to systematic absences indicated $Pna2_1$ and $Pnma$ as possibilities. The intensity statistics showed clear indications of a centrosymmetric space group for the Ge, Sn and Pb salts ($\langle E^2-1\rangle = 0.902$, 1.003, 0.918, respectively) but not for CaSrSi (0.87). However, the centric space group $Pnma$ gave the more satisfactory refinements in later steps for all four compounds. Applications of direct methods in SHELXTL revealed three separate Ca, Sr and $Tt$ positions. Absorption effects were corrected by use of the SADABS subprogram, this reducing $R$(int) values by 3.3- to 5.2-fold. The final residual $R_1$/w$R_2$ values ($I > 2\sigma(I)$) and the largest peak and hole (e Å$^{-3}$) in the final difference Fourier maps were as follows: CaSrSi, 2.40/5.74%, 0.765, −0.554; CaSrGe, 1.78/4.63%, 0.481, −0.664; CaSrSn, 2.86/7.96%, 1.866, −1.421; CaSrPb, 4.77/9.91%, 4.387, −3.033. Important aspects of the data collections and refinements are collected in Table 1. Table 2(a) gives the atomic positional and isotropic equivalent displacement parameters, and Table 2(b), the anisotropic values. Table 3 lists the important interatomic distances in the structures.

### 2.4. EHTB calculations

Extended Hückel tight binding (EHTB) band calculations were carried out using the AESAR program developed by Whangbo and co-workers [13]. The input atom parameters utilized in the calculations were as follows: Ca: 4*s* −7.0 (eV), 1.20; 4*p* −4.0, 1.20; Sr 5*s* −6.62, 1.214; 5*p* −3.92, 1.214; Si: 3*s* −17.30, 1.383; 3*p* −9.20, 1.383; Ge: 4*s* −16.0, 2.16; 4*p* −9.0, 1.85; Sn: 5*s* −16.16, 2.12; 5*p* −8.32, 1.81; Pb: 6*s* −15.7, 2.35; 5*p* −8.0, 2.06 as cited in the literature [14–18]. All these came from the compilation by Alvarez [19].

## 3. Results and discussion

### 3.1. Structures

The four compounds CaSr$Tt$, $Tt$ = Si, Ge, Sn, and Pb all crystallize in what is best described as the inverse-$PbCl_2$-type structure [20] with three characteristic crystallographic sites occupied. (Its distinction from the related $Co_2Si$ type [21] will be considered later.) The structure is illustrated in a [010] projection in Fig. 1 in which Ca, Sr, and $Tt$ atoms are distinguished as black, gray, and white spheres, respectively. The tetrel atoms roughly center confacial trigonal prisms (TPs) (outlined in gray) that share (1) triangular faces along the projection axis (*b*) to generate infinite columns and (2) two Sr–Sr side edges of each prism to form puckered sheets along *a*, leaving the third Ca–Ca edge with the smaller cation unshared. This last feature is important because it allows stronger Ca–$Tt$ bonding (see

Table 1
Crystal data and structure refinement data for CaSrSi, CaSrGe, CaSrSn, and CaSrPb

| Cmpd. | CaSrSi | CaSrGe | CaSrSn | CaSrPb |
|---|---|---|---|---|
| fw | 155.79 | 200.29 | 246.41 | 344.89 |
| Space group, $Z$ | — | *Pnma* (No. 62), 4 | — | — |
| Cell dimen. (Å, Å$^3$) | | | | |
| $a$ | 8.108(2) | 8.124(2) | 8.421(2) | 8.509(2) |
| $b$ | 4.944(1) | 4.949(1) | 5.168(1) | 5.189(1) |
| $c$ | 9.170(2) | 9.184(2) | 9.685(2) | 9.740(2) |
| $V$ | 367.6(1) | 369.3(1) | 421.4(1) | 430.1(2) |
| $d_{calcd}$ (Mg/m$^3$) | 2.815 | 3.603 | 4.854 | 5.172 |
| μ (Mo $K\alpha$) (mm$^{-1}$) | 16.104 | 23.691 | 24.439 | 52.45 |
| Crystal size (mm) | 0.1 × 0.1 × 0.15 | 0.1 × 0.15 × 0.2 | 0.08 × 0.1 × 0.15 | 0.1 × 0.1 × 0.15 |
| $F$(000) | 228 | 360 | 540 | 560 |
| $\Theta$(max) (deg.) | 28.16 | 28.20 | 28.15 | 28.24 |
| % complete | 96.2 | 96.4 | 96.5 | 96.1 |
| Refl. collected | 2143 | 2132 | 2216 | 2396 |
| Indep. obs. refl. ($R_{int}$) | 485 (0.0292) | 489 (0.0298) | 544 (0.290) | 563 (0.145) |
| Data/restr./param. | 485/0/19 | 489/0/19 | 544/0/19 | 563/0/19 |
| Goof | 1.147 | 1.121 | 1.184 | 1.012 |
| Final residuals: | | | | |
| $R_1$, w$R_2[I>2\sigma(I)]$[a] | 0.0240, 0.0574 | 0.0178, 0.0463 | 0.0286 0.0796 | 0.0477, 0.0991 |
| All data | 0.0268, 0.0583 | 0.0199, 0.0468 | 0.0372, 0.0806 | 0.0540, 0.1009 |
| Max. resid. Peaks, e/Å$^3$ | 0.765, −0.0554 | 0.481, −0.664 | 1.87, −1.42 | 4.39, −3.03 |

[a] $R_1 = \sum F_0 - F_c / \sum F_0$; $wR_2 = \sum w(F_0^2 - F_c^2)^2 / \sum [w(F_0^2)]^{1/2}$.

below). Note also that adjoining sheets along $c$ (vertical) alternate in this projection by $b/2$. This allows prismatic atoms in one sheet to function as waist-capping atoms on TPs in adjoining sheets across the gap (along $c$), which give each *Tt* atom three additional neighbors to yield the familiar tricapped trigonal prismatic (TCTP) environment. The long cation–cation basal edges of the prisms in the sheets (3.77, 3.80, 4.26 Å) are emphasized by gray connections in the figure only to aid geometric comprehension. (A comparable Sr–Sr separation across the gap (4.12 Å) is omitted in this description.) Of course, these geometric features do not represent bonds, rather the important Ca,Sr–*Tt* bonding contacts are denoted here only by the thinner black lines.

The formation of shorter and presumably stronger Ca–*Tt* interactions is doubtless why the more open and unshared positions are occupied by the smaller Ca in the TPs. (The same distinction has been seen in CaMg*Tt*, *Tt* = Sn, Pb [22], and in older work for MgCa*Tt* and MgSr*Tt*, *Tt* = Si–Pb [23].) The bond lengths around *Tt* thus fall into two groups; in the silicide these are, to Ca and Sr, respectively, 2-fold separations of 3.05 and 3.46, 3.60 Å (Sr) within the prisms plus shorter single distances of 3.08, 3.12 Å (Ca) and 3.28 Å for the face-capping modes. These distances naturally all increase for the larger and heavier *Tt*, with evidently only small differences appearing because of distortions. Interestingly, the average Sr–Si separation in this ternary is also less than in the corresponding distance in the binary $Sr_2Si$ (by 0.08 Å) [24]; that is, a closer approach of the large cation to *Tt* occurs in the presence of a second smaller one (a matrix effect), but this effect seems to disappear with the larger Sn in CaSrSn vs. $Sr_2Sn$ [25].

In detail, variations from Si to Pb in the CaSr*Tt* series naturally increases the lattice constants, volumes, and interatomic distances (Tables 1, 3), but these changes are by no means uniform along the *Tt* series. For example, the cell volumes vary as 368.3, 370.0, 422.2 and 430.9 Å$^3$, and likewise, the shorter 2-fold Ca–*Tt* distances within the prisms increase as 3.05, 3.06, 3.21 and 3.22 Å in the same order. All other distance measures evidently exhibit the same characteristic groupings, the values for Si and Ge and for Sn and Pb clearly falling into two groups with a larger difference between them. This behavior appears to be characteristic of *Tt*, as seen in their covalent radii ($r_{Si} = 1.17$ Å $> r_{Ge} = 1.24$ Å $> r_{Sn} = 1.42$ Å $> r_{Pb} = 1.50$ Å [26]). The same trend is found in more relevant estimates of $Tt^{-4}$ anionic radii according to Ca–*Tt* (monomer) separations in the related $Ca_5Tt_3$ phases with $Cr_5B_3$ structures, 2.11, 2.14, and 2.25 Å for the first three (the binary lead member does not exist, only the hydride $Ca_5Pb_3H$) [27]. The larger distance interval between Ge and Sn likely originates from the smaller than linear increase in radii for the 4th-period elements between Si and Ge because of the intrusion of the 3*d* series before the latter. Electropositive characteristics, etc. behave likewise [28].

### 3.2. Structure types

There are two general considerations about this and a related structure that may not be as familiar. The (inverse) $PbCl_2$-type structure of these $Ae_2Tt$ phases can also be described in terms of the more fundamental bonded network between the alkaline-earth metals and tetrels marked with black lines in Fig. 2, which has the same

Table 2

| Cmpd. | Atom | x | y | z | U(eq)[a] |
|---|---|---|---|---|---|
| (a) Atomic coordinates and isotropic-equivalent displacement parameters ($Å^2 \times 10^3$) for CaSrSi, CaSrGe, CaSrSn, and CaSrPb | | | | | |
| CaSrSi | Ca | 0.1488(1) | 1/4 | 0.0737(1) | 10(1) |
| | Sr | 0.0213(1) | 1/4 | 0.6785(1) | 17(1) |
| | Si | 0.2656(2) | 1/4 | 0.3937(2) | 14(1) |
| CaSrGe | Ca | 0.1481(1) | 1/4 | 0.0731(1) | 12(1) |
| | Sr | 0.0214(1) | 1/4 | 0.6785(1) | 16(1) |
| | Ge | 0.2655(1) | 1/4 | 0.3933(1) | 11(1) |
| CaSrSn | Ca | 0.1507(2) | 1/4 | 0.0708(2) | 8(1) |
| | Sr | 0.0215(1) | 1/4 | 0.6811(1) | 19(1) |
| | Sn | 0.2619(1) | 1/4 | 0.3898(1) | 16(1) |
| CaSrPb | Ca | 0.1492(4) | 1/4 | 0.0693(3) | 13(1) |
| | Sr | 0.0218(2) | 1/4 | 0.6801(2) | 20(1) |
| | Pb | 0.2622(1) | 1/4 | 0.3887(1) | 17(1) |
| | $U^{11}$ | $U^{22}$ | $U^{33}$ | $U^{23}$ | $U^{13}$ | $U^{12}$ |
| (b) Anisotropic displacement ellipsoids ($Å^2 \times 10^3$)[b] | | | | | | |
| Ca | 12(1) | 9(1) | 8(1) | 0 | 0(1) | 0 |
| Sr | 16(1) | 20(1) | 16(1) | 0 | 1(1) | 0 |
| Si | 14(1) | 14(1) | 13(1) | 0 | −1(1) | 0 |
| Ca | 15(1) | 10(1) | 11(1) | 0 | 0(1) | 0 |
| Sr | 16(1) | 18(1) | 15(1) | 0 | 1(1) | 0 |
| Ge | 13(1) | 10(1) | 11(1) | 0 | −1(1) | 0 |
| Ca | 11(1) | 6(1) | 6(1) | 0 | −2(1) | 0 |
| Sr | 17(1) | 20(1) | 18(1) | 0 | 0(1) | 0 |
| Sn | 16(1) | 14(1) | 17(1) | 0 | −1(1) | 0 |
| Ca | 14(2) | 12(1) | 12(1) | 0 | 1(1) | 0 |
| Sr | 18(1) | 24(1) | 18(1) | 0 | 0(1) | 0 |
| Pb | 17(1) | 17(1) | 17(1) | 0 | 1(1) | 0 |

[a] $U$(eq) is defined as one-third of the trace of the orthogonalized $U_{ij}$ tensor.

[b] The anisotropic displacement factor exponent takes the form: $-2\pi^2[h^2 a^{*2} U^{11} + \ldots + 2h\,k\,a^*\,b^*\,U^{12} + \ldots]$.

Table 3
Important bond lengths (Å) in CaSrSi, CaSrGe, CaSrSn, and CaSrPb

| | CaSrSi | CaSrGe | CaSrSn | CaSrPb |
|---|---|---|---|---|
| Sr–Ca | 3.804(1) | 3.813(1) | 3.963(2) | 3.994(4) |
| Sr–Ca × 2 | 3.768(1) | 3.778(1) | 3.929(2) | 3.966(3) |
| Sr–Ca | 3.767(1) | 3.767(1) | 3.928(2) | 3.943(3) |
| Sr–Ca × 2 | 3.630(1) | 3.636(1) | 3.815(2) | 3.848(3) |
| Sr–*Tt* | 3.278(2) | 3.285(1) | 3.472(1) | 3.499(2) |
| Sr–*Tt* × 2 | 3.458(1) | 3.463(1) | 3.584(1) | 3.608(1) |
| Sr–*Tt* × 2 | 3.604(1) | 3.607(1) | 3.754(1) | 3.773(1) |
| Sr–Sr | 4.261(1) | 4.269(1) | 4.372(2) | 4.379(2) |
| Ca–*Tt* | 3.121(1) | 3.124(1) | 3.296(2) | 3.318(4) |
| Ca–*Tt* | 3.083(2) | 3.092(1) | 3.228(2) | 3.256(3) |
| Ca–*Tt* × 2 | 3.052(1) | 3.057(1) | 3.208(1) | 3.224(2) |
| Ca–Ca × 2 | 3.709(1) | 3.704(1) | 3.873(3) | 3.873(5) |
| *Tt*–Ca | 3.121(2) | 3.124(1) | 3.296(2) | 3.318(4) |
| *Tt*–Ca | 3.083(2) | 3.092(1) | 3.229(2) | 3.256(3) |
| *Tt*–Ca × 2 | 3.052(1) | 3.057(1) | 3.208(1) | 3.224(2) |
| *Tt*–Sr | 3.278(2) | 3.285(1) | 3.472(1) | 3.499(2) |
| *Tt*–Sr × 2 | 3.458(1) | 3.463(1) | 3.584(1) | 3.608(1) |
| *Tt*–Sr × 2 | 3.604(1) | 3.607(1) | 3.754(1) | 3.773(1) |

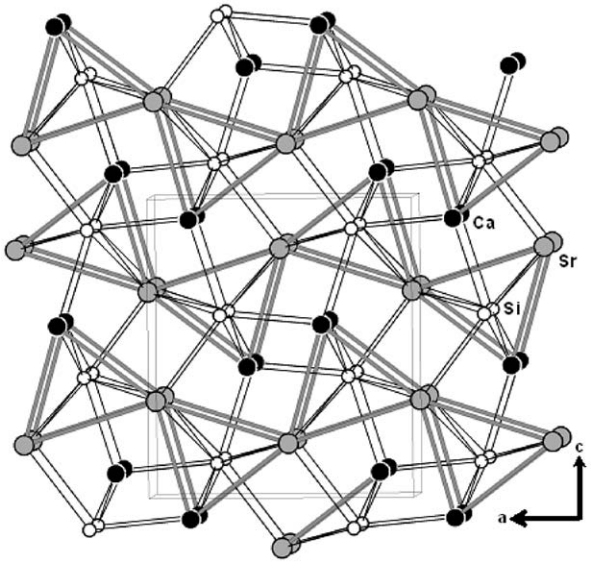


Fig. 1. [010] View of the *inverse*-$PbCl_2$-type crystal structure of CaSr*Tt* (*Tt* = Si, Ge, Sn, Pb). The Ca, Sr and Si atoms are black, gray, and white, respectively. The columns of edge-sharing trigonal prisms along the projection are outlined in gray to emphasize the geometry, whereas the important bonding contacts between Si and Ca or Sr are marked in black. Note that the horizontal sheets of trigonal prisms alternate by $b/2$ in the vertical ($c$) direction.

orientation as Fig. 1. This arrangement can also be seen to consist of a three-dimensional network of (distorted) edge-sharing square-pyramidal $Tt_5$ groups (dashed lines) centered by Sr atoms, the Ca atoms falling in tetrahedral voids in the *Tt* sublattice. Note that these dashed lines mark only geometrical features and not significant bonding interactions. (Again, atoms in the top half of this drawing differ from those below by $b/2$, giving some irregularities in the arrangement of square pyramids vertically.)

Another structure sometimes confused with, or not always distinguished from, the inverse-$PbCl_2$ type is that of $Co_2Si$. Several mapping analyses have shown that these two can generally, but not always, be separated in terms of lattice dimension ratios, $a/b$ being particularly discriminating [29,30]. The larger ratios for $PbCl_2$ members also allow a further differentiation, as follows. As Miller and Cheng noted [31], the present *inverse*-$PbCl_2$ structure type is generally adopted by compounds in which the forces between the majority atoms (Cl, *Ae*, etc.) are not bonding, rather closed shell or repulsive, and the coordination numbers of cations about the centering atom therein (Pb, *Tt*) are consistently as found here, four (Ca) and five (Sr) among the two independent positions. The $Co_2Si$ type with generally lower $a/b$ axial ratios and more attractive covalent (metal–metal) interactions between the Co-type atoms typically leads to an increased coordination of the Si-like centered atom by the majority atom type that is not shared between TCTP (Co2) [30]. For $Co_2Si$ as an example, the additional coordination of

Si follows a topological distortion within the sheets (chains) along $a$ [100]; the decrease in $a/b$ causes the horizontal sheets to pucker and intermesh more and thereby generate two Co2 neighbors across the gap rather than one (with Ca). This is readily seen in Fig. 3 in a view and design of the $Co_2Si$-type structure ($[0, \bar{1}, 0]$, $\frac{1}{2}, 0, 0$) that is comparable to that in Fig. 1 but with the additional Co2–Si contacts marked with heavier black lines. The increased puckering on decrease of $a/b$ is also reflected in the angles along the edges of the TP chain, Fig. 3, those for 1–2–3 and the following 2–3–4 decreasing by 18.8–142.4° and increasing by 6.8–94.8° between the CaSrSi and $Co_2Si$ examples, respectively. (Note also the greater displacement of the Si atom from the center of the TCTP.)

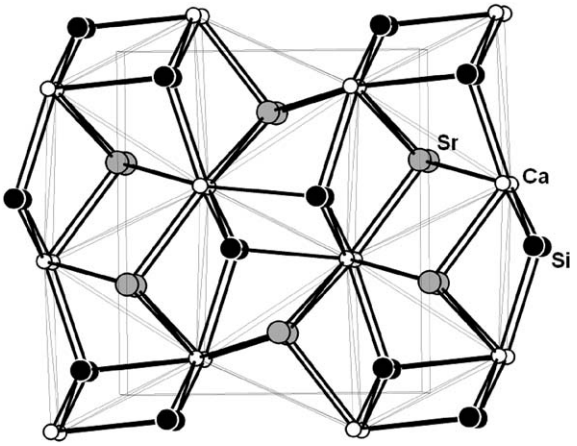


Fig. 2. Alternate [010] view of the structure of CaSr*Tt* with the strong *Ae*–*Tt* interactions marked in black. The long *Tt*–*Tt* separations (dashed light lines) define a geometric lattice of edge-sharing $Tt_5$ square pyramids that enclose the Sr atoms, whereas the Ca atoms lie in tetrahedral $Tt_4$ cavities. The atom legend is the same as in Fig. 1.

### 3.3. Chemical bonding and electronic structure

Electronic band structures have been calculated for the isotypic CaSrSi, CaSrGe, CaSrSn and CaSrPb by means of the EHTB method. Fig. 4 shows the total and the projected contributions to the densities-of-states (DOS) (left) and the crystal orbital overlap population (COOP) data (right) for CaSrSi. These results alone are sufficient because they remain very similar down the rest of the *Tt* group, although

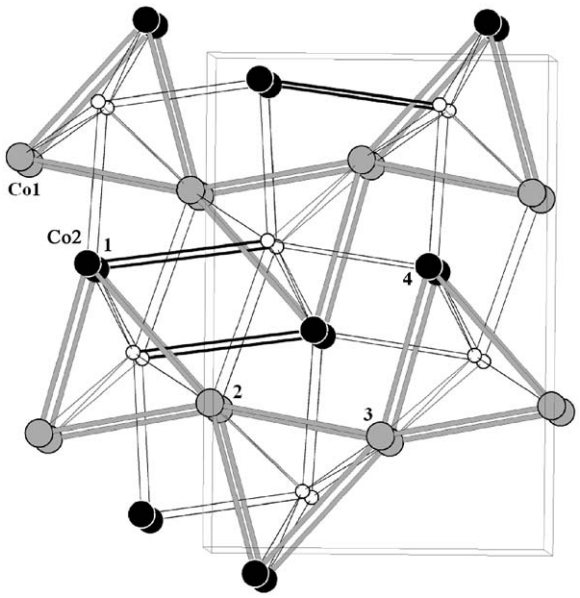


Fig. 3. The $Co_2Si$ structure in a view corresponding to that of the $PbCl_2$ type in Fig. 1. Note that Si is now 5-bonded to Co2. The added Si–Co contacts that arise because of greater interpenetration of adjoining puckered sheets are marked by wider black lines. The numbers 1–4 define angles discussed in the text.

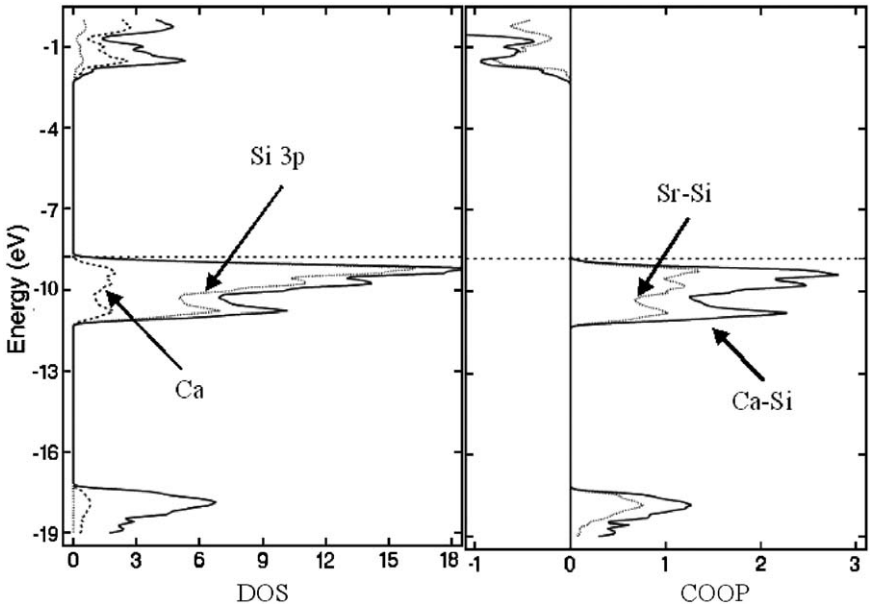


Fig. 4. Densities-of-states (DOS) and the crystal orbital overlap population (COOP) data for CaSrSi according to EHTB calculations, with contributions as marked. The DOS states around −18 eV arise mainly from Si 3*s* orbitals.

the prominent valence band does broaden somewhat for the heavier *Tt* and, in parallel, the Sr–*Tt* COOP results likewise become more similar to those for Ca–*Tt*. A total of 32 valence electrons per cell ($Z = 4$) fill the states up to a Fermi energy for CaSrSi of −8.7 eV. The lowest DOS contribution originates mainly from *Tt s* states. A gap of about 6 eV separates this from the wider valence band in which *Tt p*, Ca *s*,*p* and Sr *s*,*p* states play the dominant roles. An optical gap of ~6.7–5.4 eV is predicted for the series, although EHTB methods usually exaggerate this feature. The ab initio calculations for the isotypic $Ca_2Tt$ compounds [32] are doubtless more accurate in this respect and show gaps in the range of about 0.6–0.15 eV down the group. A semiconduction property is expected for the present phases as well, although our measurement results were not so conclusive (Section 2).

## References


[1] J.D. Corbett, in: S.M. Kauzlarich (Ed.), Chemistry, Structure and Bonding of Zintl Phases and Ions, VCH Publishers, New York, 1996 (Chapter 4).
[2] J.D. Corbett, Angew. Chem. Int. Ed. 39 (2000) 670.
[3] Z.-C. Dong, J.D. Corbett, J. Am. Chem. Soc. 117 6447.
[4] S.C. Sevov, J.D. Corbett, Inorg. Chem. 32 (1993) 1612.
[5] W. Carrillo-Cabrera, N. Caroca-Canales, H.-G. von Schnering, Z. Anorg. Allg. Chem. 620 (1994) 247.
[6] D.-K. Seo, J.D. Corbett, J. Am. Chem. Soc. 122 (2000) 9621.
[7] S. Liu, J.D. Corbett, Inorg. Chem. 43 (2004) 4988.
[8] A.K. Ganguli, J.D. Corbett, M. Köckerling, J. Am. Chem. Soc. 120 (1998) 1223.
[9] A.K. Ganguli, S. Gupta, J.-T. Zhao, E.A. Leon-Escamilla, J.D. Corbett, J. Solid State Chem. 178 (2005) 2959.
[10] J.T. Zhao, J.D. Corbett, Inorg. Chem. 34 (1995) 378.
[11] SMART, Bruker AXS, Inc., Madison, WI, 1996.
[12] SHELXTL, version 5.1, Bruker AXS, Inc., Madison, WI, 1998.
[13] J. Ren, W.,Liang, M.-H. Whangbo, CAESAR for Windows, Prime-Color Software, Inc., North Carolina State University, Raleigh, NC, 1998.
[14] C. Zheng, R. Hoffmann, J. Am. Chem. Soc. 108 (1986) 3078.
[15] J. Hinze, H.H. Jaffe, J. Chem. Phys. 67 (1963) 1501.
[16] N. Trong Anh, M. Elian, R. Hoffmann, J. Am. Chem. Soc. 100 (1978) 110.
[17] L. Thom, R. Hoffmann, Inorg. Chem. 17 (1978) 126.
[18] E. Canadell, O. Eisenstein, T. Hughbanks, Inorg. Chem. 23 (1984) 2435.
[19] A. Alvarez, Tables of Parameters for Extended Hückel Calculations, Parts 1 and 2, Barcelona, Spain, 1987.
[20] K. Sahl, Beitr: Mineral. Petrogr. 9 (1963) 111.
[21] S. Geller, Acta Crystallogr. 8 (1955) 83.
[22] A.K. Ganguli, A.M. Guloy, J.D. Corbett, J. Solid State Chem. 152 (2000) 474.
[23] B. Eisenmann, H. Schäfer, A. Weiss, Z. Anorg. Allg. Chem. 391 (1972) 241.
[24] A. Widera, B. Eisenmann, H. Schäfer, Z. Naturforsch. 31B (1976) 520.
[25] A. Widera, H. Schäfer, J. Less-Common Met. 77 (1981) 29.
[26] L. Pauling, Nature of the Chemical Bond, third ed., Cornell University Press, Ithaca, NY, 1960, p. 403.
[27] E.A. Leon-Escamilla, J.D. Corbett, J. Solid State Chem. 159 (2001) 149.
[28] N.N. Greenwood, A. Earnshaw, Chemistry of the Elements, second ed., Butterworth-Heinemann, London, 1997, pp. 220, 371.
[29] W. Jeitschko, Acta Crystallogr. B 24 (1968) 930.
[30] F. Flahaut, F. Thévet, J. Solid State Chem. 32 (1980) 365.
[31] G.J. Miller, J. Cheng, Inorg. Chem. 34 (1995) 2962.
[32] D.M. Migas, L. Miglio, V.I. Shaposhnikov, V.E. Borisenko, Phys. Rev. B 67 (2003) 205203.